

# Probing the chemistry of adhesion between a 316L substrate and spin-on-glass coating

**Lampert, Felix; Kadkhodazadeh, Shima; Kasama, Takeshi; Dahl, Kristian Vinter; Christiansen, Alexander Bruun; Møller, Per**

*Published in:*
Langmuir

*Link to article, DOI:*
10.1021/acs.langmuir.7b03131

*Publication date:*
2018

*Document Version*
Peer reviewed version

Article

# Probing the chemistry of adhesion between a 316L substrate and spin-on-glass coating

Felix Lampert, Shima Kadkhodazadeh, Takeshi Kasama, Kristian Vinter Dahl, Alexander Bruun Christiansen, and Per Møller

*Langmuir*, **Just Accepted Manuscript** • DOI: 10.1021/acs.langmuir.7b03131 • Publication Date (Web): 19 Feb 2018

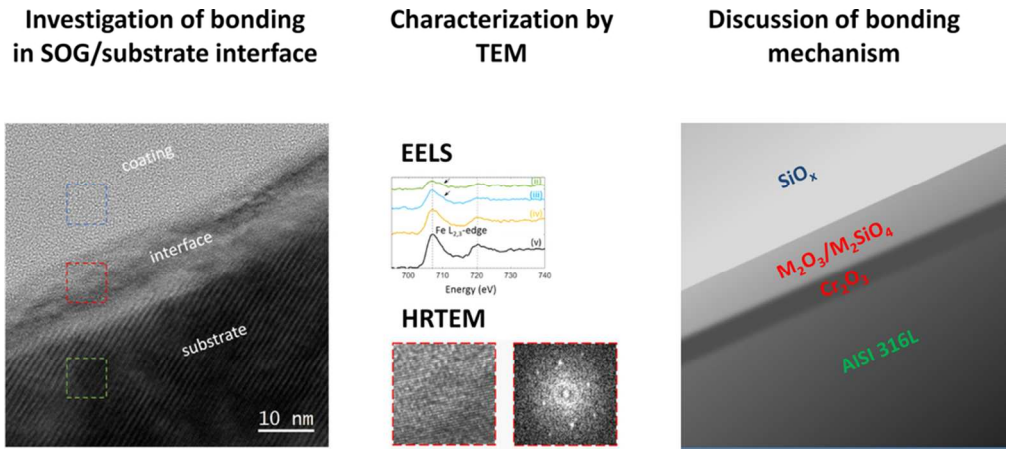


Table of Contents/Abstract Graphic

87x38mm (300 x 300 DPI)

# Probing the chemistry of adhesion between a 316L substrate and spin-on-glass coating

Felix Lampert[a], Shima Kadkhodazadeh[b], Takeshi Kasama[b], Kristian Vinter Dahl[a], Alexander Bruun Christiansen[c], Per Møller[a]

[a] Technical University of Denmark, Department of Mechanical Engineering, Produktionstorvet 425, 2800 Kgs. Lyngby, Denmark

[b] Technical University of Denmark, Center for Electron Nanoscopy (CEN), Fysikvej 307, 2800 Kgs. Lyngby, Denmark

[c] SiOx ApS, Bybjergvej 7, 3600 Espergærde, Denmark

## Abstract

Hydrogen silsesquioxane ($[HSiO_{3/2}]_n$) based "spin-on-glass" has been deposited on 316L substrate and cured in $Ar/H_2$ gas atmosphere at 600 ºC to form a continuous surface coating with sub-micrometer thickness. The coating functionality depends primarily on the adhesion to the substrate, which is largely affected by the chemical interaction at the interface between the coating and the substrate. We have investigated this interface by transmission electron microscopy and electron energy loss spectroscopy. The analysis identified a 5-10 nm thick interaction zone containing signals from O, Si, Cr and Fe. Analysis of the energy loss near edge structure of the present elements identified predominantly signal from $[SiO_4]^{4-}$ units together with $Fe^{2+}$, $Cr^{2+}$ and traces of $Cr^{3+}$. High-resolution transmission electron microscopy images of the interface region confirm a crystalline $Fe_2SiO_4$ interfacial region. In agreement with computational thermodynamics, it is proposed that the spin-on-glass forms a chemically bonded silicate-rich interaction zone with the substrate. It was further suggested that this zone is composed of a corundum-type oxide at the substrate surface, followed by an olivine-

structure intermediate phase and a spinel-type oxide in the outer regions of the interfacial zone.

## 1 Introduction

Due to their inherent resistance towards galvanic corrosion combined with good formability, austenitic stainless steels belong to the most widely used engineering materials. Apart from the chemical composition and the mechanical/thermal history, the functionality of the materials is greatly determined by the surface finish, and hence their surface modification plays a major role in the development of improved stainless steel engineering components. Over the recent years, intense research effort has been directed into the surface modification by $SiO_x$-based micrometer/sub-micrometer thick coatings to improve the wear resistance[1,2], biocompatibility[3,4], bio fouling characteristics and cleanability[5,6], surface morphology[7–10] and corrosion resistance in saline[11–13], acid[11,14,15] or high temperature[16] environments of stainless steel components at a minimal impact on the component geometry. Apart from the traditional deposition processes, such as chemical vapor deposition[17], physical vapor deposition[18], sol-gel processing[19] or liquid phase deposition[20], the deposition from hydrogen silsesquioxane (HSQ), $[HSiO_{3/2}]_n$, spin-on-glass (SOG) has shown excellent results for the processing of high quality $SiO_x$-like thin films[21,22]. In addition to the deposition of near stoichiometric silica films, SOG-technology offers the possibility to deposit fully inorganic films with various degrees hydrogenation as intermediate reaction products, resulting in a broad range of film properties[21–23]. While the material was mainly developed for microelectronics applications[23,24] or as electron beam resist[25], it has recently emerged into the surface finishing industry and shown an outstanding performance as coating material for metallic substrates such as aluminum or tool steel[7–10].

Recently, we have shown the applicability of SOG as material for sub-micrometer thick coatings on stainless steel substrates[26–28]. Our studies have proven the concept of precursor deposition by an industrially applicable dip-coating process and the subsequent coating curing in both oxidizing[27,28] and non-oxidizing[26] atmosphere, showing that both processes may yield well adherent coatings with 200-400 nm thickness on substrates with 2B finish[29]; however, we have also demonstrated that the coating efficiently levels the substrate surface, and thus fills substrate defects (e.g. surface voids), which may consequently lead to a local increase in coating thickness exceeding 1400 nm[26]. Further, we have shown that oxidative curing induces thermal oxidation of the substrate[27], leading to adhesive failure of the coating and ultimately to functional component failure[28]. We have reported that the formation of a thick, detrimental interface was driven by an abundance of oxygen in the curing atmosphere[27], and that the formation of a thick interfacial zone can be suppressed by a removal of oxygen from the curing atmosphere, i.e. by curing in a non-oxidizing atmosphere such as Formiergas[26]. However, the methods applied in the previous work were inadequate to clearly resolve the interface between the coating and the substrate and, hence, the interfacial chemistry, morphology and the bonding mechanism between coating and substrate are unclear.

In agreement with other studies[11,13,30–35], our previous findings[27,28] emphasize the significance of the coating/substrate interface for both the adhesion and the performance of glass coatings on stainless steel. However, to the author's knowledge, previous studies have generally focused on the formation of thick interface oxides[31–33], traditional enameling technology of complex industrial porcelains[30] or on vapor deposition techniques[34,35], which may lead to significantly different bonding mechanisms. Consequently, the interface formation of well adherent, non-oxidatively cured HSQ-based coatings cannot be adequately deduced based on previous literature. Hence, the present study aims at a detailed characterization of the interfacial chemistry of non-oxidatively cured SOG on type 316L substrate by Transmission

Electron Microscopy (TEM). The interface was characterized by electron energy loss spectroscopy in scanning-TEM together with and high resolution TEM and the analytical results are discussed based on the thermodynamical oxide/metal phase equilibrium at the interface. This analysis provides novel insights into the metal-glass bonding mechanism of silica-like coatings on stainless steel substrate and, in conclusion, the adhesive performance of the coatings.

## 2 Experimental section

To analyze the bonding mechanism between a stainless steel substrate and a SOG coating, AISI 316L substrates (composition in Table I) with no. 2B surface finish were coated with HSQ-based SOG by the method previously described in Lampert *et al.*[26]: The test coupons were dip coated in commercial HSQ-solution (Dow Corning FOx 25) and subjected to a two stage heat treatment, the first step being a soft bake at 160 ºC in air and the second a polymerization at 600 ºC under flow of 0.5 l/min $Ar/H_2$ gas mixture (10 vol.% $H_2$) for 2h. The temperature of the polymerization stage was elevated with respect to our previous work[26] in order to decrease the susceptibility of the coating material to ionizing irradiation [36] during ion beam milling and the TEM investigation.

Lamellae for TEM investigations were prepared by focused ion beam (FIB) milling in a FEI Helios NanoLab 600 dual beam scanning electron microscope (SEM). The specimens were first sputter coated with 20-30 nm of Au to avoid surface charging during the FIB preparation, followed by in-situ deposition of a Pt layer prior to milling to protect the sample from irradiation damage. FIB-milling was carried out at 30 kV ion beam accelerating voltage, followed by final polishing at 2 kV ion beam accelerating voltage and 0.44 nA ion beam current. The lamellae were additionally polished in a Fischione NanoMill precision Ar-ion mill (500 V accelerating voltage and 100 pA beam current) to remove the residual FIB

damage. The TEM examination of the samples was performed in a FEI Titan 80-300kV instrument fitted with a FEG electron source, a monochromator and a GIF Tridiem electron energy loss spectroscopy (EELS) spectrometer. Scanning-TEM (STEM) -EELS measurements were carried out at 120 kV accelerating voltage. In STEM, spatial resolutions of 5 Å and 1.5 Å, respectively with and without the monochromator excited, were obtained. The EELS measurements were acquired with the monochromator excited and had an energy resolution of 0.15 eV. High-resolution TEM (HRTEM) imaging was carried out at 300 kV and with the point to point resolution of 1.4 Å. Thermodynamic phase equilibrium calculations were performed in Thermo-Calc version 2017a[37] using version 7.0 of the Thermo-Calc Software steel database TCFE. The elements Fe, Cr, Mn, Ni, Si and O were considered in the calculations.

## 3 Results and Discussion

A high-angle annular dark-field (HAADF) STEM image of the coating – substrate cross-section is shown in Figure 1(a). Image intensity in HAADF STEM is primarily related to the atomic number (Z-contrast) of the material, indicating an interfacial region distinct from the coating and the substrate (labelled "interface"). This is similar to our previous investigation of an oxidatively cured coating[27], where an interfacial reaction zone was detected. Here, a much thinner interfacial zone of 5 – 10 nm is detected, compared to in the oxidatively cured coating. EELS line scans spanning energy ranges 400 – 1000 eV (covering the O K-edge and Cr, Mn, Fe and Ni $L_{2,3}$-edges) and 90 – 150 eV (containing the Si $L_{2,3}$-edge) were acquired from the coating/substrate interface, in order to probe the chemistry of this interfacial zone. The Si $L_{2,3}$-edge had to be recorded separately, as our experimental setup limits the spectral energy range to 600 eV at most, and thus we were unable to record all edges of interest together in the same spectrum. The relative composition profile of O, Cr and Fe calculated from the EEL spectra along with the HAADF intensity profile and the intensity of the Si signal along a line across

the interface are plotted in Figure 1(b). Approximate boundaries for the substrate and the coating, determined from the changes in the HAADF image intensity profile along the recorded line scans, are marked in the graphs. We were unable to analyze the composition profile of Ni, due to the pronounced overlap between the Ni $L_{2,3}$-edge and the Fe $L_1$-edge. The detection of the Mn $L_{2,3}$-edge was also hindered due to its low concentration and low signal level in the measurements. The measurements were repeated across different regions of the sample and were found to be reproducible. As evident in the graphs in Figure 1(b) the constituent elements have relatively unchanged concentrations in the substrate and the coating. An interfacial zone of approximately 6 nm, containing all four elements Fe, Cr, O and Si is detected. The concentrations of Fe and Cr in the interface decrease from the substrate towards the coating and those of O and Si increase.

The energy-loss near-edge fine-structure (ELNES) in EELS is a powerful tool in probing the local chemistry of a sample, containing information such as chemical bonding, oxidation state, crystal structure and coordination[38]. EEL spectra recorded at different points along the interface are plotted in Figure 2(a) (O, Cr, Fe) and Figure 2(b) (Si). Here we analyze the ELNES of the spectra in different regions:

**Coating.** The signal acquired in the coating contains the Si L- and the O K-edges. The ELNES in both the Si $L_{2,3}$- and O K-edges in this region (spectra at position (i)) resemble closely those for amorphous $SiO_2$ with $SiO_4$ tetrahedral networks[39–41]: the Si $L_{2,3}$-edge contains three main peaks at ~ 106 eV, ~ 108 eV and ~ 115 eV. The first peak corresponds to 2p to unoccupied s-type states in Si and its onset has been shown to vary from ~ 100 eV for $Si^0$ to ~ 103 eV for $Si^{2+}$ to ~ 105 eV for $Si^{4+}$ [42]. The peaks at 108 eV and 115 eV arise from 2p to dominantly d-type states, and are influenced by the Si – O tetrahedral coordination in silica[39,40]. The O K-edge in the coating features a main peak at ~ 537 eV and a broad peak at ~ 560 eV.

**Interface.** The spectra acquired in the interface contains signals from Si, O, Cr and Fe. Little change is observed in the fine structure of Si $L_{2,3}$-edge at position (ii) in the interface relative to the coating. This indicates the continued dominant presence of $[SiO_4]^{4-}$ units in the interface. The splitting in the initial peak at 106 eV, due to spin-orbit coupling of 2p electrons in Si, can be clearly resolved here[41,43]. A pre-peak at ~ 103 eV appears in the spectra at positions (iii) and (iv). The reduced onset energy of the Si $L_{2,3}$ edge signifies a lower oxidation number of Si at these positions, which may be related to the presence of Fe and Cr in the interface, *e.g.* due to the formation of olivine ($Me_2SiO_4$)-structure phases such as $Fe_2SiO_4$[39] or Cr-bearing Si sub-oxides[40]. The O K-edges from positions (ii) and (iii) have overall similar profiles to that acquired in the coating. The first peak at ~ 537 eV arises mainly from scattering of excited electrons (from 1s state in O) by second nearest O neighbors and beyond[44] and has been shown to have little dependence on *e.g.* the Si – O – Si bond angle[45,46]. The peak at ~ 560 eV has been shown to shift to lower energies with increasing Si – O bond length (*i.e.* reduced ionic character)[44]. Such a shift is observed in the O K-edge at position (ii) and (iii). Additionally, the peak at ~ 537 eV in the spectra acquired at positions (ii), (iii) and (iv) contains a shoulder on the right hand side, indicating a larger crystal field effect[47] compared to position (i). This could be the result of distortion or change in the structure of the interface relative to the coating. A decrease in the onset energy of the O K-edge and a hint of a pre-peak can be seen in the spectra at positions (iii) and (iv). A pre-peak is typically present in the ELNES of the O K-edge of transition metal oxides[48,49] and a similar decrease in onset energy of the O K-edge can be observed for silicates such as $Fe_2SiO_4$ (fayalite)[50]. The $L_{2,3}$ edges of transition metals reveal valuable information regarding their oxidation state, crystal structure and chemical environment. For example, the position of the $L_2$ and $L_3$ peaks are shown to be sensitive to their oxidation and shift typically to higher energies with increasing oxidation state[49,51–54]. The intensity ratio of $L_3/L_2$ edges in transition metals is another important parameter related to the d-orbital occupancy (and subsequently

the oxidation state). Each of the $L_2$ and $L_3$ peaks can also contain fine details, stemming from crystal field effects, which provide further clues to the chemical state of the transition metal[49,51,54]. The peak maxima of the Fe $L_3$ and $L_2$ here are positioned respectively at ~ 707 eV and ~ 720 eV, without showing any noticeable change across the interface (see spectra (ii) – (iv)). The average integrated intensity of $L_3/L_2$ edges of Fe in the interface region determined according to the method described by van Aken *et al.*[47] is 3.5 ($L_3/L_2$ ratio in the substrate is ~ 2.8). Both the peak maxima energies and the $L_3/L_2$ ratio in the interface region correspond well to those for $Fe^{2+}$ [47,49,51,55]. The fine structure present on the Fe $L_{2,3}$ edge across the interface is also consistent with this observation: A splitting in the $L_3$ edge (marked with arrows in spectra (ii) and (iii) of Fe $L_{2,3}$ edges in Figure 2(a)) can be resolved, characterized by a small bump at ~ 710 eV after the main peak[47,49,51]. We thus conclude that the Fe present in the interface region is predominantly in $Fe^{2+}$ state. In the case of Cr, small shifts in the $L_3$ peak maxima at different points across the interface are detected. The measured $L_3$ and $L_2$ peak maxima at position (iii) of ~ 576 eV and ~ 585 eV correspond closely to $Cr^{2+}$ [52,54]. Although the fine structure on the Cr $L_3$ edge cannot be clearly resolved in our measurements, its overall profile at position (iii) also suggests the presence of $Cr^{2+}$ [52,54]. In comparison, the Cr $L_3$ peaks at positions (ii) and (iv) have their maxima at slightly higher energies (approximately 1.0 eV and 0.6 eV shifts at positions (ii) and (iv), respectively). Their overall shapes also varies compared to the Cr $L_{2,3}$ edge at position (iii): this is in particular clear at position (ii), where Cr $L_3$ has a longer tail to the left of its main peak, suggesting that $Cr^{3+}$ may also be present[52,54].

**Substrate.** The spectra collected from the substrate contain signals from Fe and Cr in metallic form.

A reasonable hypothesis based on the results of our ELNES analysis of the interface is that it is composed of $Fe_2SiO_4$, $Cr_2SiO_4$ and small amounts of $Cr^{3+}$-rich oxides such as $Cr_2O_3$ or

$Cr^{3+}$-bearing spinel, which have previously been reported as high temperature oxides of CrNi steels[56]. High-resolution TEM (HRTEM) images of the structure reveals that the interface is crystalline (see also Figure S1 in the supporting information (SI)). A HRTEM image of the substrate – coating structure with fast Fourier transform (FFT) patterns corresponding to regions within each of the substrate, interface and the coating are depicted in Figure 3. The crystalline nature of the substrate and the interface can be clearly seen in the image. However, the FFT patterns obtained from the substrate and the interface regions are distinctly different, indicating that the two regions have different crystal structures. Although not in a low-index zone-axis orientation, the FFT pattern of the interface is compatible with a $Fe_2SiO_4$ structure (see Figure S2 in the SI).

The interface formation is expected to resemble the thermal oxidation of the substrate at low oxygen partial pressure ($O_2$ pp.) and elevated Si-access, whereby the $O_2$ pp. is expected to show a decrease from the outer region of the interface (e.g. position (ii) in Figure 2) to its inner region (e.g. position (iv) in Figure 2). Thus, the interface formation has been simulated by computation of the phase equilibrium of the substrate composition vs. $O_2$ pp. at 600 ºC at elevated Si-level (for the computation a Si content of 2 wt.% has been assumed). The respective property diagram showing the phase equilibrium is shown in Figure 4. Clearly, the oxide-phase equilibrium is dominated by a Fe/Cr/Ni/Mn-rich spinel-structure oxide ($M_3O_4$), together with an Fe/Cr-rich corundum-structure oxide ($M_2O_3$) at high $O_2$ pp. and a stoichiometric $Cr_2O_3$ (corundum-structure) at low $O_2$ pp., which generally agrees with the medium temperature oxides that have been experimentally identified after the oxidation of CrNi steel[56]. Neither of the previously discussed phases is enriched in Si. Si is entirely bound in form of quartz ($SiO_2$) over a broad range of $O_2$ pp. or a Fe-rich olivine-structure phase at medium $O_2$ pp. (i.e. fayalite). Overall, the equilibrium calculation supports the hypothesis of fayalite formation in the interfacial zone together with the formation of $Cr_2O_3$ directly at the substrate surface, where the lowest $O_2$ pp. is expected. Further, the calculated phase

equilibrium is in agreement with the observation of $Cr^{3+}$ in the outer region of the interfacial zone, which may be bound in a spinel-type oxide where the highest $O_2$ pp. is expected. Since no trace of $Fe^{3+}$ was evident from the experiment, we propose that the formation of an outer corundum-structure layer was suppressed by the low oxygen availability during the thermal treatment. The formation of a thin, chemically bonded interfacial zone has been previously linked to good adhesion between glasses and metals[35,40]. Hence, the herein presented formation of a silicate-rich interaction zone may be directly linked to the adhesion of the coating, and thus prevent coating spallation and ensure an excellent performance and mechanical durability of SOG based coatings in industrial applications[57]. Further, the formation of a silicate-rich interface zone has been related to an increased corrosion resistance[11], and thus the herein observed interfacial zone may have a strong positive impact on the corrosion behavior of the coating system. A detailed study of the performance of SOG coatings on stainless steel substrates including a discussion of the impact of the herein reported interface layer will be the content of following investigations.

## 4 Summary and Conclusions

In summary, we investigated the chemistry of the interface between AISI 316L and SOG coating using STEM-EELS and HRTEM imaging. An interfacial region of ~ 10 nm thickness, containing Si, O, Cr and Fe was detected. Analysis of the ELNES indicated these elements to be in $Fe^{2+}$, $Cr^{2+}$ (as well as, small amounts of $Cr^{3+}$) and $[SiO_4]^{4-}$ forms. HRTEM images of the structure reveals that the interface is crystalline, with the FFT patterns matching a $Fe_2SiO_4$ (fayalite) -structure. The experimental results have been validated by thermodynamics simulations and we suggest that thermal processing of the SOG leads to the formation of a chemical interaction zone with the substrate which may generate excellent adhesion of the coating.

## Acknowledgements

This work is funded by Innovation Fund Denmark under grant number 50-2014-1. The authors acknowledge SiOx Aps, Denmark, for the deposition of the coatings and all other project partners. The A. P. Møller and Chastine Mc-Kinney Møller Foundation is gratefully acknowledged for their contribution toward the establishment of the Centre for Electron Nanoscopy at the Technical University of Denmark.

## References

(1) Garzino-Demo, G. A.; Lama, F. L. Friction and Wear of Uncoated or SiO2-Coated 329 Stainless Steel and of Uncoated or A1N-Coated Aluminium Surfaces. *Surf. Coatings Technol.* **1994**, *68/69*, 507–511.

(2) Gallardo, J.; Duran, A.; Garcia, I.; Celis, J. P.; Arenas, M. A.; Conde, A. Effect of Sintering Temperature on the Corrosion and Wear Behavior of Protective SiO2-Based Sol-Gel Coatings. *J. Sol-Gel Sci. Technol.* **2003**, *27*, 175–183.

(3) Walke, W.; Paszenda, Z.; Basiaga, M.; Karasinski, P.; Kaczmarek, M. EIS Study of SiO2 Oxide Film on 316L Stainless Steel for Cardiac Implants. In *Information Technologies in Biomedicine, Vol 4.*; Piętka, E., Kawa, J., Wieclawek, W., Eds.; Advances in Intelligent Systems and Computing; Springer International Publishing: Cham, 2014; Vol. 283, pp 403–410.

(4) Walke, W.; Paszenda, Z.; Pustelny, T.; Opilski, Z.; Drewniak, S.; Ko, M.; Basiaga, M. Evaluation of Physicochemical Properties of SiO2-Coated Stainless Steel after Sterilization. *Mater. Sci. Eng. C* **2016**, *63*, 155–163.

(5) Santos, O.; Nylander, T.; Rosmaninho, R.; Rizzo, G.; Yiantsios, S.; Andritsos, N.; Karabelas, A.; Müller-Steinhagen, H.; Melo, L.; Boulangé-Petermann, L.; et al. Modified Stainless Steel Surfaces Targeted to Reduce Fouling—surface

Characterization. *J. Food Eng.* **2004**, *64* (1), 63–79.

(6) Rosmaninho, R.; Santos, O.; Nylander, T.; Paulsson, M.; Beuf, M.; Benezech, T.; Yiantsios, S.; Andritsos, N.; Karabelas, A.; Rizzo, G.; et al. Modified Stainless Steel Surfaces Targeted to Reduce Fouling – Evaluation of Fouling by Milk Components. *J. Food Eng.* **2007**, *80* (4), 1176–1187.

(7) Mohaghegh, K.; Hansen, H. N.; Pranov, H.; Kofod, G. A Study on the Surface Roughness of a Thin HSQ Coating on a Fine Milled Surface. In *14th euspen International Conference - Dubrovink*; 2014.

(8) Mohaghegh, K.; Hansen, H. N.; Pranov, H.; Kofod, G. Verification of Thickness and Surface Roughness of a Thin Film Transparent Coating. In *Proceedings of the 13th euspen International Conference*; Berlin, 2013.

(9) Cech, J.; Pranov, H.; Kofod, G.; Matschuk, M.; Murthy, S.; Taboryski, R. Surface Roughness Reduction Using Spray-Coated Hydrogen Silsesquioxane Reflow. *Appl. Surf. Sci.* **2013**, *280*, 424–430.

(10) Hobæk, T. C.; Matschuk, M.; Kafka, J.; Pranov, H. J.; Larsen, N. B. Hydrogen Silsesquioxane Mold Coatings for Improved Replication of Nanopatterns by Injection Molding. *J. Micromechanics Microengineering* **2015**, *25* (3), 035018 (9pp).

(11) Vasconcelos, D. C. L.; Carvalho, J. A. N.; Mantel, M.; Vasconcelos, W. L. Corrosion Resistance of Stainless Steel Coated with Sol–gel Silica. *J. Non. Cryst. Solids* **2000**, *273* (1–3), 135–139.

(12) Hwang, T.; Lee, H.; Kim, H.; Kim, G. Two Layered Silica Protective Film Made by a Spray-and-Dip Coating Method on 304 Stainless Steel. *J. Sol-Gel Sci. Technol.* **2010**, *55* (2), 207–212.

(13) Pech, D.; Steyer, P.; Millet, J.-P. Electrochemical Behaviour Enhancement of Stainless

Steels by a SiO2 PACVD Coating. *Corros. Sci.* **2008**, *50* (5), 1492–1497.

(14) Atik, M.; de Lima Neto, P.; Avaca, L. A.; Aegerter, M. A.; Zarzycki, J. Protection of 316L Stainless Steel against Corrosion by SiO2 Coatings. *J. Mater. Sci. Lett.* **1994**, *13* (15), 1081–1085.

(15) de Sanctis, O.; Gomez, L.; Pellegri, N.; Parodi, C.; Marajofsky, A.; Duran, A. Protective Glass Coatings on Metallic Substrates. *J. Non. Cryst. Solids* **1990**, *121*, 338–343.

(16) de Sanctis, O.; Gomez, L.; Pellegri, N.; Duran, A. Behaviour in Hot Ammonia Atmosphere of SiO2-Coated Stainless Steels Produced by a Sol-Gel Procedure. *Surf. Coatings Technol.* **1995**, *70*, 251–255.

(17) Foggiato, J. Chemical Vapor Deposition of Silicon Dioxide Films. In *Handbook of Thin Film Deposition Processes and Techniques (Second Edition)*; Elsevier B.V., 2001; pp 111–149.

(18) Møller, P.; Nielsen, L. P. Physical Vapor Deposition. In *Advanced Surface Technology, Vol 1*; 2013; pp 457–482.

(19) Brinker, C. J.; Scherer, G. W. Hyrdolysis and Condensation of Silicon Alkoxides. In *Sol-Gel Science*; Academic Press, Inc.: San Diego, 1990; pp 108–216.

(20) Nagayama, H.; Honda, H.; Kawahara, H. A New Process for Silica Coating. *J. Electrochem. Soc.* **1988**, *135* (8), 2013–2016.

(21) Többen, D.; Weigand, P.; Shapiro, M. J.; Cohen, S. A. Influence of the Cure Process on the Properties of Hydrogen Silsesquioxane Spin-on-Glass. *Mater. Res. Soc. Somposium Proc.* **1997**, *443*, 195–200.

(22) Loboda, M. J.; Grove, C. M.; Schneider, R. F. Properties of a-SiOx:H Thin Films Deposited Form Hydrogen Silsesquioxane Resins. *J. Electrochem. Soc.* **1998**, *145* (8),

2861–2866.

(23) Siew, Y. K.; Sarkar, G.; Hu, X.; Hui, J.; See, A.; Chua, C. T. Thermal Curing of Hydrogen Silsesquioxane. *J. Electrochem. Soc.* **2000**, *147* (1), 335.

(24) Bremmer, J. N.; Liu, Y.; Gruszynski, K. G.; Dall, F. C. Cure of Hydrogen Silsesquioxane for Intermetal Dielectric Applications. *Mater. Res. Soc. Symp. Proc.* **1997**, *476*, 37–44.

(25) Choi, S. K. Nanolitography and Nanofabrication Using Hydrogen Silsesquioxane Resists (Dissertation), University of Illinois, 2009.

(26) Lampert, F.; Jensen, A. H.; Din, R. U.; Møller, P. Hydrogen Silsesquioxane Based Silica Glass Coatings for the Corrosion Protection of Austenitic Stainless Steel. *Surf. Coatings Technol.* **2016**, *307*, 879–885.

(27) Lampert, F.; Kadkhodazadeh, S.; Jensen, A. H.; Din, R. U.; Møller, P. Interfacial Interaction of Oxidatively Cured Hydrogen Silsesquioxane Spin-On-Glass Enamel with Stainless Steel Substrate. *J. Electrochem. Soc.* **2017**, *164* (6), C231–C239.

(28) Lampert, F.; Christiansen, A. B.; Din, R. U.; Gonzalez-Garcia, Y.; Møller, P. Corrosion Resistance of AISI 316L Coated with an Air-Cured Hydrogen Silsesquioxane Based Spin-On-Glass Enamel in Chloride Environment. *Corros. Sci.* **2017**, *127*, 110–119.

(29) ASTM Standard A480/A480M 14b: Standard Specification for General Requirements for Flat-Rolled Stainless and Heat- Resisting Steel Plate, Sheet, and Strip. ASTM International: West Conshohocken 2016, pp 1–26.

(30) Shieu, F. S.; Deng, M. J.; Lin, K. C.; Wong, J. C.; Wu, J. Y. Effect of Surface Pretreatments on the Adherence of Porcelain Enamel to a Type 316L Stainless Steel. *J. Mater. Sci.* **1999**, *34*, 5265–5272.

(31) Stoch, A.; Stoch, J.; Rakowska, A. An XPS and SEMS Study of Silica Sol-Gel/metal

Substrate Interaction. *Surf. Interface Anal.* **1994**, *22*, 242–247.

(32) Takemori, M. Crack Formation, Exfoliation, and Ridge Formation in 500 $^{o}$C Annealed Sol-Gel Silica Coatings on Stainless Steel SUS304: Part I. Microscopic Observations and Elemental Analysis. *Ceram. Int.* **2009**, *35*, 1731–1746.

(33) Takemori, M. Crack Formation, Exfoliation, and Ridge Formation in 500 °C Annealed Sol–gel Silica Coatings on Stainless Steel SUS304: Part II Spectroscopic and Mechanical Analyses and Insights into Mechanisms Controlling Coating Characteristics. *Ceram. Int.* **2009**, *35* (5), 1747–1755.

(34) Onyiriuka, E. C.; Kinney, L. D.; Binkowski, N. J. Adhesion and Delamination of Tantalum and Chromium Films on Glass. *J. Adhes. Sci. Technol.* **1997**, *11* (7), 929–940.

(35) Benjamin, P.; Weaver, C. The Adhesion of Evaporated Metal Films on Glass. *Proc. R. Soc. London. Ser. A, Math. Phys.* **1961**, *261* (1307), 516–531.

(36) Peuker, M.; Lim, M. H.; Smith, H. I.; Morton, R.; van Langen-Suurling, A. K.; Romijn, J.; van der Drift, E. W. J. M.; van Delft, F. C. M. J. M. Hydrogen SilsesQuioxane, a High-Resolution Negative Tone E-Beam Resist, Investigated for Its Applicability in Photon-Based Lithographies. *Microelectron. Eng.* **2002**, *61–62*, 803–809.

(37) Andersson, J. O.; Helander, T.; Höglund, L.; Shi, P. F.; Sundman, B. Thermo-Calc and DICTRA, Computational Tools for Materials Science. *Calphad* **2002**, *26*, 273–312.

(38) Keast, V. J.; Bruley, J. Electron Energy-Loss near-Edge Structure - a Tool for the Investigation of Electronic Structure on the Nanometre Scale. *J. Microsc.* **2001**, *203* (August), 135–175.

(39) Garvie, L. A. G.; Useck, P. R. Bonding in Silicates : Investigation of the Si L 2 , 3 Edge by Parallel Electron Energy-Loss Spectroscopy. *Am. Mineral.* **1999**, *84*, 946–964.

(40) Jiang, N.; Silcox, J.; Jiang, N.; Silcox, J. Observations of Reaction Zones at Chromium / Oxide Glass Interfaces. *J. Appl. Phys.* **2000**, *87* (8), 3768.

(41) Batson, P. E. Atomic Resolution Electronic Structure in Silicon-Based Semiconductors. *J. Electron Microsc. (Tokyo).* **1996**, *45* (1), 51–58.

(42) Batson, P. E. Simultaneous STEM Imaging and Electron Energy-Loss Spectroscopy with Atomic-Column Sensitivity. *Nature* **1993**, *366*, 727–728.

(43) Krivanek, O. L.; Lovejoy, T. C.; Dellby, N.; Carpenter, R. W. Monochromated STEM with a 30 meV-Wide , Atom-Sized Electron Probe. *Microscopy* **2013**, *62* (1), 3–21.

(44) Wallis, D. J.; Gaskell, P. H.; Brydson, R. Oxygen K near-Edge Spectra of Amorphous Silicon Suboxides. *J. Microsc.* **1986**, *180* (3), 307–312.

(45) Davoli, I.; Paris, E.; Stizza, E.; Benfatto, S.; Fanfoni, M.; Gargano, M.; Bianconi, A.; Seifert, F. Structure of Densified Vitreous Silica : Silicon and Oxygen XANES Spectra and Multiple Scattering Calculations. *Phys. Chem. Miner.* **1992**, *19* (3), 171–175.

(46) Brown, G. E.; Waychunas, G. A.; Stohr, J.; Sette, F. Near-Edge Structure of Oxygen in Inorganic Oxides: Effect of Local Geometry and Cation Type. *Le J. Phys. Colloq.* **1986**, *47* (C8), C8-685-C8-689.

(47) van Aken, P. A.; Liebscher, B. Quantification of Ferrous / Ferric Ratios in Minerals : New Evaluation Schemes of Fe L 23 Electron Energy-Loss near-Edge Spectra. *Phys. Chem. Miner.* **2002**, *29*, 188–200.

(48) Krivanek, O. L.; Paterson, J. H. ELNES of Transition Metal Oxides I. Variations across the Periodic Table. *Ultramicroscopy* **1990**, *32*, 313–318.

(49) Paterson, J. H.; Krivanek, O. L. ELNES OF 3d TRANSITION-METAL OXIDES 2. Variations with Oxidation State and Crystal Structure. *Ultramicroscopy* **1990**, *32*, 319–325.

(50) Garvie, L. A. G. Can Electron Energy-Loss Spectroscopy (EELS) Be Used to Quantify Hydrogen in Minerals from the O K Edge? *Am. Mineral.* **2010**, *95*, 92–97.

(51) Tan, H.; Verbeeck, J.; Abakumov, A.; Van Tendeloo, G. Oxidation State and Chemical Shift Investigation in Transition Metal Oxides by EELS. *Ultramicroscopy* **2012**, *116*, 24–33.

(52) Arévalo-López, A. M.; Alario-Franco, M. A. Reliable Method for Determining the Oxidation State in Chromium Oxides. *Inorg. Chem.* **2009**, *48* (24), 11843–11846.

(53) Malinsky, M. D.; Kelly, K. L.; Schatz, G. C.; Van Duyne, R. P. Nanosphere Lithography: Effect of Substrate on the Localized Surface Plasmon Resonance Spectrum of Silver Nanoparticles. *J. Phys. Chem. B* **2001**, *105*, 2343–2350.

(54) Stoyanov, E.; Langenhorst, F. The Effect of Valence State and Site Geometry on Cr L3,2 Electron Energy-Loss Spectra of Cr-Bearing Oxidic Compounds. *Chemie der Erde - Geochemistry* **2014**, *74* (3), 497–505.

(55) de Groot, F. M. F.; Fuggle, J. C.; Thole, B. T.; Sawatzky, G. A. 2p X-Ray Absorption of 3d Transition-Metal Compounds: An Atomic Multiplet Description Including the Crystal Field. *Phys. Rev. B* **1990**, *42* (9), 5459–5468.

(56) Lussana, D.; Baldissin, D.; Massazza, M.; Baricco, M. Thermodynamic and Kinetics Aspects of High Temperature Oxidation on a 304L Stainless Steel. *Oxid. Met.* **2014**, *81* (5–6), 515–528.

(57) Lee, G. H.; Cailler, M.; Constantinescu, C.; Kwon, S. C. Adhesion Studies of Radio-Frequency Sputtered SiO2 Films on Ti, Stainless Steel, Ni and Inconel Substrates. Effects of Substrate Surface Ion Bombardment Etching. *J. Adhes. Sci. Technol.* **1990**, *4* (6), 481–501.

## Tables

**Table I:** Chemical composition of the substrates (by Optical Emission Spectroscopy). In addition, traces (< 0.1 wt.%; > 0.01 wt.%) of P, Nb, V, W were also detected.

| **Element** | **Cr** | **Ni** | **Mo** | **Mn** | **Si** | **Cu** | **Co** | **N** | **C** | **Fe** |
|---|---|---|---|---|---|---|---|---|---|---|
| **Composition (wt.%)** | 16.8 | 10.4 | 2.07 | 0.92 | 0.47 | 0.41 | 0.21 | 0.048 | 0.019 | bal. |

## Figure Captions

**Figure 1:** (a) HAADF STEM images of the coating on AISI 316L substrates in the cross-sectional geometry. (b) Relative composition profiles of O, Cr and Fe and the Si signal intensity across the interface extracted from EELS plotted together with the intensity profile of the HAADF STEM image along the line the EEL spectra were acquired from.

**Figure 2:** EELS spectra along a line across the coating – AISI 316L interface containing the (a) O K-, Cr $L_{2,3}$- and Fe $L_{2,3}$-edges and (b) Si $L_{2,3}$-edge.

**Figure 3:** HRTEM image of the coating – AISI 316L interface, with FFT patterns of selected regions from the coating, interface and the substrate.

**Figure 4:** Phase equilibrium vs. $O_2$ partial pressure diagram of the substrate composition at increased (2 wt.%) Si-level. The property diagram was computed with Thermo-Calc Software version 2017a[37], TCFE7.0.

# Figures

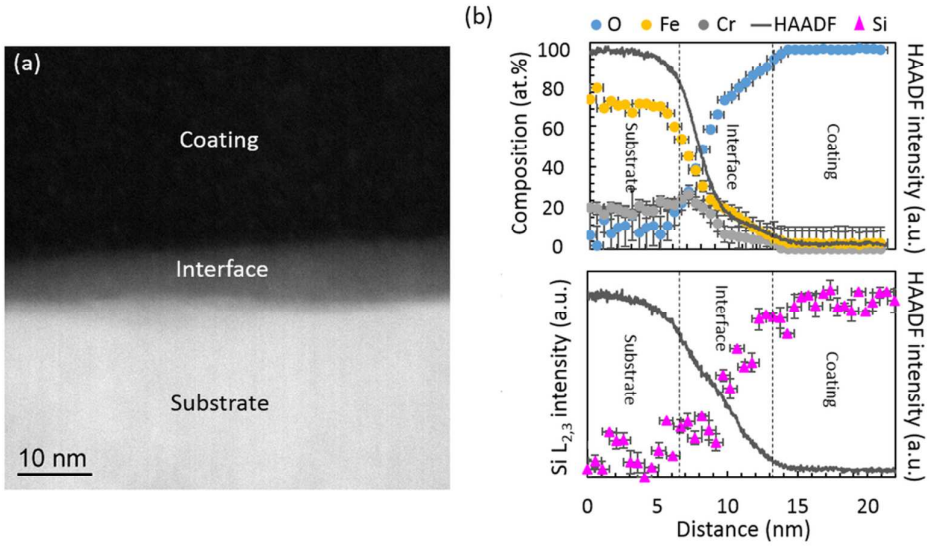


Figure 1

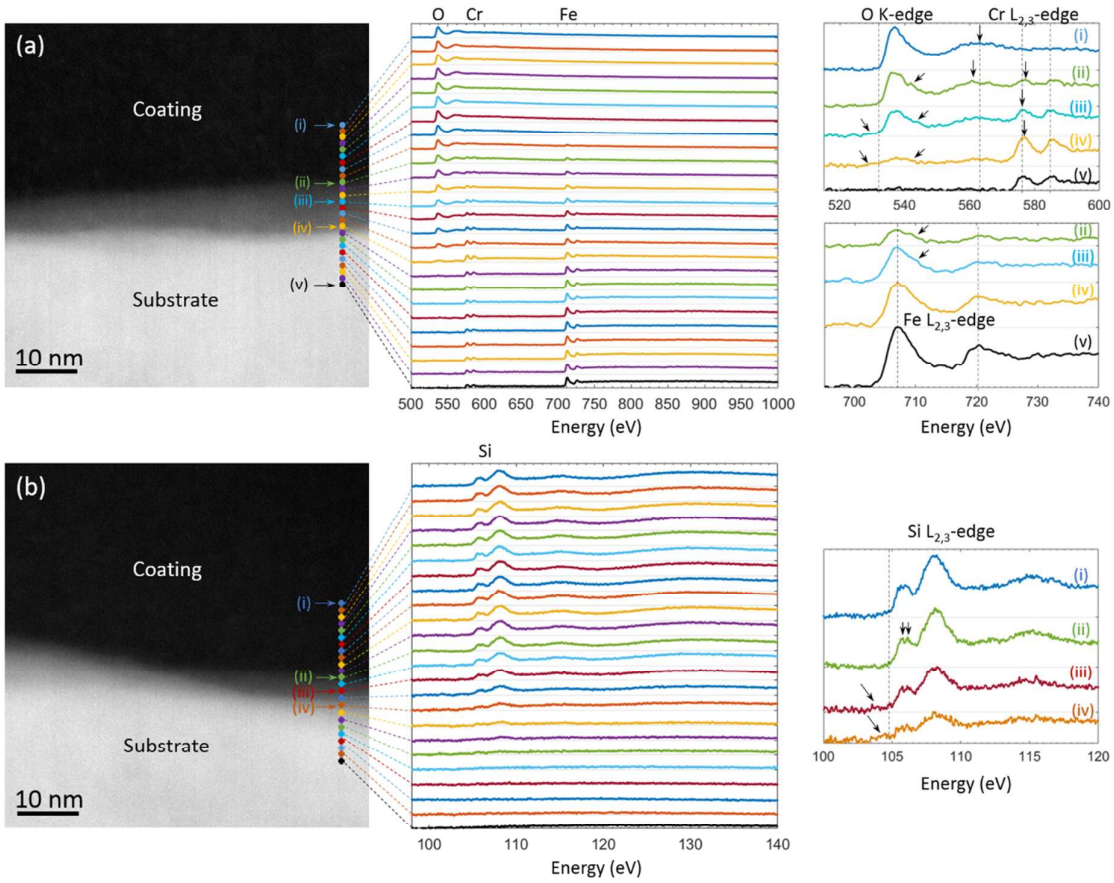
(a)
Coating
Substrate
10 nm
(i)
(ii)
(iii)
(iv)
(v)
O
Cr
Fe
500 550 600 650 700 750 800 850 900 950 1000
Energy (eV)
O K-edge
Cr L2,3-edge
520 540 560 580 600
Fe L2,3-edge
700 710 720 730 740
Energy (eV)
(b)
Coating
Substrate
10 nm
Si
100 110 120 130 140
Energy (eV)
Si L2,3-edge
100 105 110 115 120
Energy (eV)

Figure 2

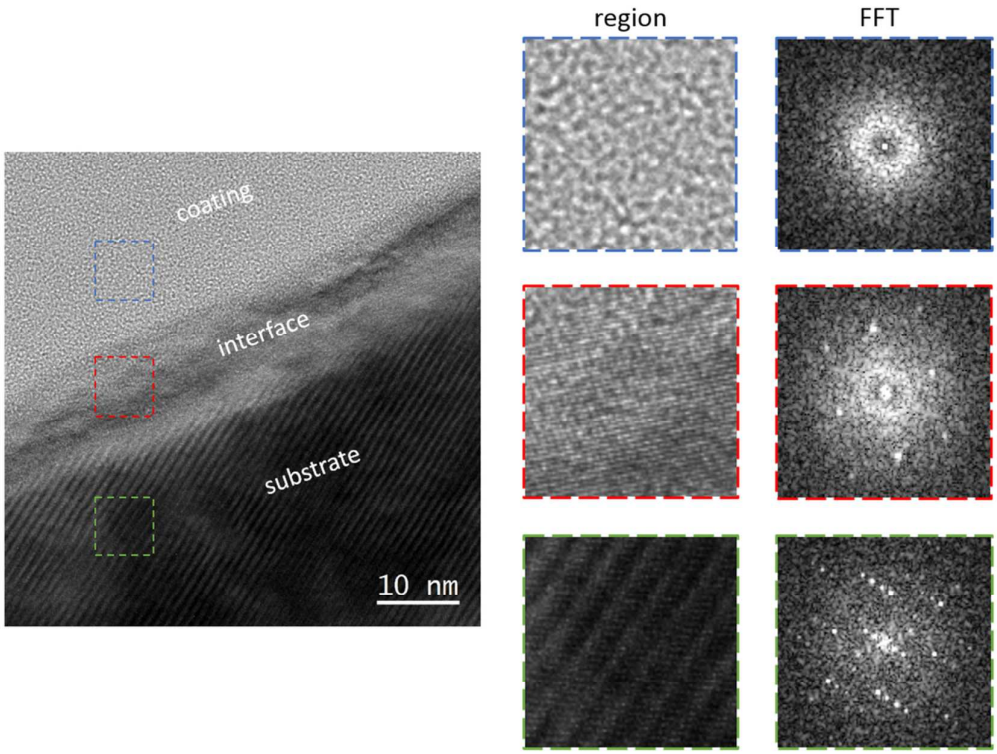


Figure 3

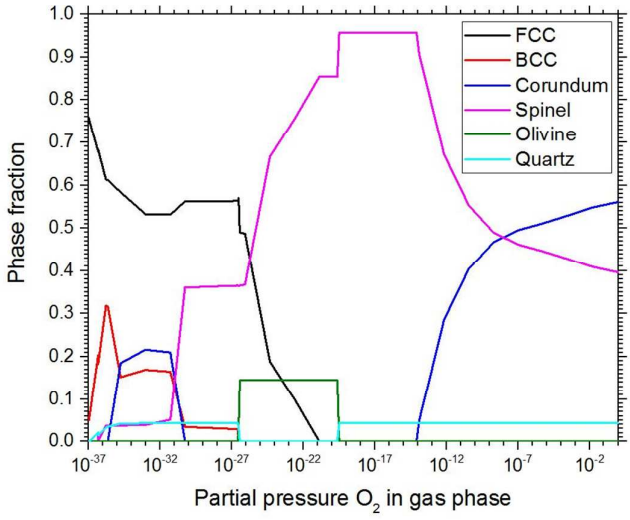
FCC
BCC
Corundum
Spinel
Olivine
Quartz
Phase fraction
Partial pressure $O_2$ in gas phase

Figure 4